

Adsorption Dynamics and Desorption Kinetics of Argon and Methane on MgO(100)<sup>†</sup>

Z. Dohnálek, R. Scott Smith, and Bruce D. Kay\*

*W. R. Wiley Environmental Molecular Sciences Laboratory, Pacific Northwest National Laboratory, 902 Battelle Boulevard, P.O. Box 999, MSN K8-88, Richland, Washington 99352**Received: April 3, 2002; In Final Form: June 3, 2002*

The adsorption dynamics and desorption kinetics of Ar and CH<sub>4</sub> on MgO(100) are studied using a combination of molecular beam scattering and temperature-programmed desorption (TPD). Both Ar and CH<sub>4</sub> exhibit an initial trapping probability that decreases dramatically with increasing kinetic energy and is independent of incident angle indicating a barrierless process obeying total energy scaling. The trapping probability for both systems increases roughly linearly with increasing adsorbate coverage in the first layer. Analysis of the TPD spectra yields desorption energies of 8.5 and 13 kJ/mol for Ar and CH<sub>4</sub>, respectively.

## I. Introduction

The dynamics and kinetics of adsorption and desorption of molecules from surfaces play an important role in many heterogeneous processes having both fundamental and technological importance. Catalysis, gaseous corrosion, and microelectronics fabrication, for example, are processes that involve reactive gas–surface scattering with enormous economic and strategic importance. Nonreactive gas–surface interactions form the atomistic basis for such macroscopically relevant phenomena as aerodynamic drag and heat transfer. Over the past 2 decades, considerable experimental and theoretical progress has been made in understanding the dynamics of both molecular<sup>1–16</sup> and dissociative<sup>17–25</sup> adsorption on metal surfaces.

While the structure and thermodynamic properties of adsorbates on metal oxide surfaces<sup>26</sup> have been explored using a broad range of experimental and theoretical techniques, the dynamics and kinetics of adsorbate–metal oxide interactions are not well understood. For example, even the dynamics relevant to the physisorption of weakly bound species on well-ordered single-crystal oxide surfaces is largely unexplored.<sup>27–31</sup> The paucity of experimental dynamical studies is related to difficulties in the preparation of ordered, high-quality oxide surfaces, as well as problems associated with the rapid cooling of these low thermal conductivity crystals. To circumvent these problems, we employ high-quality MgO(100) thin films, grown epitaxially on Mo(100).<sup>32,33</sup> Procedures for the growth and characterization of these MgO(100) films are presented elsewhere.<sup>28</sup>

Here, we report the results of experiments employing a combination of molecular beam scattering and temperature-programmed desorption (TPD) techniques to study the adsorption dynamics and desorption kinetics of Ar and CH<sub>4</sub> on high-quality MgO(100). For both Ar and CH<sub>4</sub>, the initial trapping probability decreases dramatically with increasing kinetic energy. Furthermore, for a fixed kinetic energy, the trapping probability does not depend on the incident angle of the impinging beam flux. Together these findings indicate that the initial trapping probability exhibits total energy scaling. This is very likely due to the presence of a potential energy surface

having a large degree of lateral corrugation, consistent with recent theoretical calculations on these systems.<sup>34,35</sup> The trapping probability also exhibits an interesting dependence upon adsorbate coverage, increasing with increasing surface coverage. This finding is analogous to recent observations of Carlsson and Madix for Ar and CH<sub>4</sub> on Pt(111), systems for which the initial trapping probability exhibits so-called normal energy scaling.<sup>13</sup> Analysis of the TPD spectra yields desorption energies of  $8.5 \pm 1.4$  and  $13 \pm 2$  kJ/mol for Ar and CH<sub>4</sub> on MgO(100), respectively. These energies are in excellent agreement with previously published values based on experimental measurements<sup>35–39</sup> and theoretical calculations.<sup>34,35</sup>

## II. Experimental Section

The experiments were conducted in an ultrahigh vacuum (UHV) chamber with a base pressure of  $\sim 1 \times 10^{-10}$  Torr. The Mo(100) substrate was cleaned using a standard procedure involving a sequence of O<sub>2</sub> annealing at 1500 K (5 min,  $1 \times 10^{-6}$  Torr of O<sub>2</sub>) to remove mainly carbon contamination, and subsequent e-beam heating in UHV to 2100 K.<sup>40</sup> The temperature of the substrate was measured using a W–5% Re/W–26% Re thermocouple and could be varied under computer control from 20 to 1500 K. An absolute temperature calibration was performed using the multilayer desorption of various gases (N<sub>2</sub>, Ar, O<sub>2</sub>, and H<sub>2</sub>O) from the sample surface.<sup>41</sup> The resulting uncertainty in the absolute temperature is estimated to be  $\pm 2$  K. The surface purity and order of the Mo(100) substrate and the MgO(100) thin films were checked using Auger electron spectroscopy (AES) and low-energy electron diffraction (LEED).

Thin MgO(100) films were grown epitaxially on the Mo(100) substrate at 600 K by evaporation of Mg metal in an O<sub>2</sub> atmosphere ( $P_{O_2} = 1 \times 10^{-6}$  Torr).<sup>32,33</sup> Complete oxidation of the Mg in the film was confirmed by the absence of the metallic Mg<sup>0</sup>(LVV) feature in the AES spectrum at 44 eV.<sup>32,33</sup> The Mg ribbon (Aldrich, 99%) was placed into an Al<sub>2</sub>O<sub>3</sub> tube that was closed on one side. A W wire was tightly wrapped around the tube to allow for heating of the whole assembly. The temperature of the tube was measured using a type K thermocouple cemented on to the closed side of the tube. The whole doser assembly was placed inside a Ta shield to achieve directional Mg dosing. The film thickness was calibrated using TPD of the Mg monolayer from clean Mo(100). This calibration assumes that

<sup>†</sup> Part of the special issue "John C. Tully Festschrift".

\* To whom correspondence should be addressed. E-mail: Bruce.Kay@pnl.gov.

the sticking of Mg on the Mo(100) substrate and the MgO-(100) films is the same. On the basis of this calibration, the deposition rate used to grow the MgO films in this study was  $\sim 0.5$  ML/min. Repeated annealing of the MgO(100) films up to 1100 K did not cause any change in the LEED pattern for the clean surface or in the TPD spectra of various adsorbates, indicating that the films are thermally stable. All experiments were performed on thick MgO films (40–80 ML) to ensure good quality of the MgO(100) surface.<sup>28</sup> Because the quality of the MgO(100) surface is characterized using LEED and N<sub>2</sub> or CO TPD,<sup>28</sup> any inaccuracy in the absolute film thickness determination caused by unknown sticking coefficient of Mg on Mo(100) and MgO(100) will not affect the results presented here.

Supersonic beams of Ar and CH<sub>4</sub> were generated by expanding the pure gases (Air Liquide, research grade) through a 100  $\mu$ m diameter nozzle at a backing pressure of roughly 500 Torr. The kinetic energy of the resultant supersonic beam was varied by changing the temperature of the nozzle assembly through a combination of resistive heating and liquid nitrogen cooling. The nozzle temperature,  $T_n$ , could be varied between 85 and 1000 K and was controlled to a precision of  $\pm 1$  K during any given adsorption experiment. The translational energies of Ar and CH<sub>4</sub> were calculated using the relations  $E_{Ar} = \frac{5}{2}RT_n$  and  $E_{CH_4} = \frac{7}{2}RT_n$ , respectively. These relationships are in accord with velocity distributions determined previously<sup>42</sup> using time-of-flight methods<sup>43,44</sup> to analyze Ar and CH<sub>4</sub> expansions from an identical nozzle under similar expansion conditions. These expansion conditions give rise to relatively narrow velocity distributions,  $v/\Delta v(\text{fwhm}) > 10$ , and correspond to kinetic energy distributions having  $E/\Delta E(\text{fwhm}) > 5$ . The variable-energy supersonic beam is quadruply differentially pumped prior to impinging on the MgO(100) target where it illuminates a diameter of  $\sim 5$  mm at normal incidence. Typical beam fluxes employed in this study were roughly  $10^{14}$  cm<sup>-2</sup> sec<sup>-1</sup>. The impingement angle of the incident beam can be varied continuously through angles in excess of 60° with respect to the MgO-(100) surface normal without overfilling the target. The adsorption kinetics were monitored using the beam reflection technique of King and Wells.<sup>45</sup> The details of the evaluation procedure are described elsewhere.<sup>28,46</sup>

The desorption kinetics of Ar and CH<sub>4</sub> from MgO(100) were measured using TPD in a line-of-sight arrangement with a quadrupole mass spectrometer. The dynamic range resulting from this detection configuration, when used in conjunction with molecular beam dosing, is greater than 4 decades allowing for the reliable detection of desorption rates as low as  $10^{-4}$  ML/s. All TPD spectra were acquired using a linear temperature ramp rate of 0.6 K/s. The Ar and CH<sub>4</sub> coverages are defined relative to the area under the desorption curves of saturated monolayer states. The overall shape of the TPD spectra is independent of incident-beam translational energy and impingement angle.

### III. Results and Discussion

**A. Temperature-Programmed Desorption.** The desorption kinetics of Ar and CH<sub>4</sub> are studied using TPD. Line-of-sight TPD spectra for various initial coverages of Ar and CH<sub>4</sub> are displayed in Figure 1, parts a and b, respectively. Relative coverages and desorption rates are obtained by normalizing the areas under the desorption curves relative to the area under the desorption spectrum exhibiting saturation of the monolayer state for Ar (peak at  $\sim 34$  K) and CH<sub>4</sub> (peak at  $\sim 49$  K).

The TPD spectra for Ar (Figure 1a) exhibit two distinct peaks at  $\sim 34$  and  $\sim 30$  K, which correspond to desorption from the

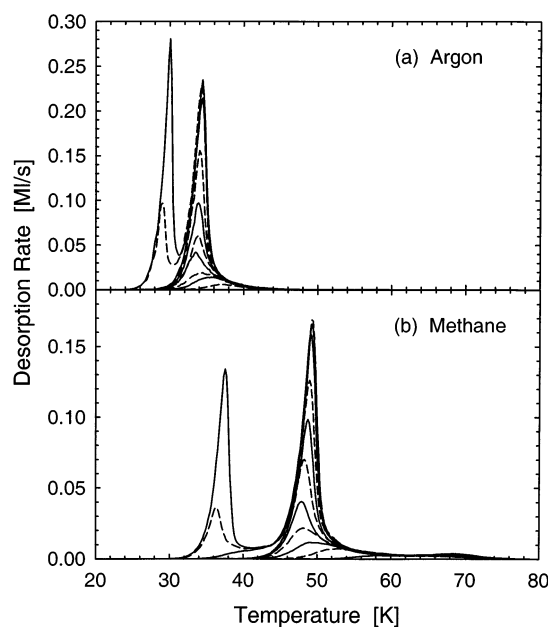


**Figure 1.** TPD spectra of various coverages of Ar (a) and CH<sub>4</sub> (b) on MgO(100). The desorption spectra shown represent coverages from 0 to  $\sim 2$  ML and are obtained with a ramp rate of 0.6 K/s after adsorption at 22 K. For clarity, the dashed and solid lines alternate between doses with increasing coverage.

first and second layer of Ar on MgO(100), respectively. Increased exposure gives rise to the formation of a nonsaturable, multilayer state (not shown) that appears at even lower temperature. For low coverages ( $\Theta < 0.2$  ML), the observed desorption maximum is shifted to higher temperatures ( $T > 34$  K) indicating preferential binding on a different type of surface site. We observe a similar shift of the low-coverage TPD peak to higher temperature for a variety of other adsorbates (CH<sub>4</sub>, CO, N<sub>2</sub>, O<sub>2</sub>, Kr, Xe) on MgO(100).<sup>28,47,48</sup> This effect is due to the presence of surface defects, such as steps and kinks, and is discussed in detail in our previous study of CO adsorption on MgO(100).<sup>28</sup>

The TPD for CH<sub>4</sub> (Figure 1b) exhibits a two-peak structure analogous to that observed for Ar/MgO(100). For CH<sub>4</sub>, both the monolayer ( $\sim 49$  K) and second layer ( $\sim 37$  K) TPD peaks are shifted to higher temperatures indicating that CH<sub>4</sub> binds to MgO(100) more strongly than Ar does. This observation is fully consistent with the fact that the polarizability of CH<sub>4</sub> ( $2.59 \times 10^{-24}$  cm<sup>3</sup>) is significantly greater than that of Ar ( $1.64 \times 10^{-24}$  cm<sup>3</sup>).<sup>49</sup> In contrast to Ar/MgO(100), the desorption of CH<sub>4</sub> from defects appears as a distinct TPD peak appearing at higher temperature (60–70 K).

The TPD spectra for both Ar and CH<sub>4</sub> can be analyzed to extract the coverage-dependent binding energy of these adsorbates to MgO(100). This analysis involves direct mathematical inversion of the TPD spectra using the Polanyi–Wigner equation,<sup>50</sup>  $-d\Theta/dt = \nu \exp[-E(\Theta)/(RT)]\Theta^n$ , where  $\Theta$  is the adsorbate coverage,  $t$  is the time,  $\nu$  is the preexponential factor for desorption,  $n$  is the order of desorption,  $E$  is the activation energy of desorption,  $R$  is the gas constant, and  $T$  is the temperature.  $T$  and  $t$  are related through the heating rate,  $\beta = dT/dt$ . A coverage-dependent desorption energy is obtained by iteratively solving this equation assuming first-order desorption kinetics and a coverage-independent preexponential factor. A detailed description of this procedure is given in our previous study of CO/MgO(100).<sup>28</sup>

Figure 2 displays the coverage-dependent desorption energies for submonolayer coverages of Ar and CH<sub>4</sub> physisorbed to

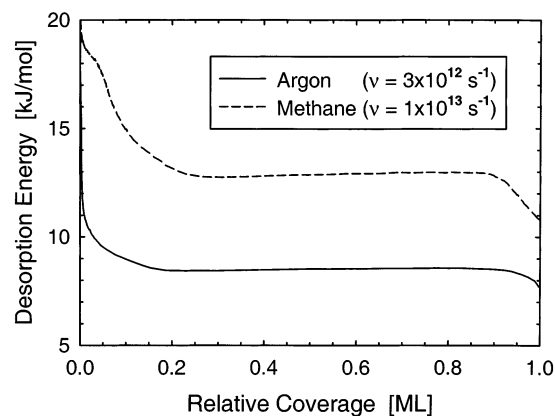


**Figure 2.** Coverage-dependent desorption energies for Ar and CH<sub>4</sub> on MgO(100). These energies were determined via inversion of the TPD spectra shown in Figure 1 assuming first-order desorption and coverage-independent preexponential factors of  $3 \times 10^{12} \text{ s}^{-1}$  (Ar) and  $1 \times 10^{13} \text{ s}^{-1}$  (CH<sub>4</sub>). Relative coverages are determined with respect to saturation of the high-temperature desorption feature observed in the TPD.

MgO(100). The coverage-independent prefactors determined from this analysis are  $3 \times 10^{12 \pm 2}$  and  $1 \times 10^{13 \pm 2} \text{ s}^{-1}$  for Ar and CH<sub>4</sub>, respectively. Although not shown here, TPD spectra simulated using the extracted kinetic parameters are in excellent agreement with the experimentally observed TPD spectra displayed in Figure 1. At low coverages, both Ar and CH<sub>4</sub> preferentially bind to surface defects indicating that the mobility of both adsorbates is sufficient to diffuse to and bind at the defects. Once the defects become saturated, the desorption energies plateau to nearly coverage-independent ( $0.2 < \Theta < 0.9$ ) values of  $8.5 \pm 1.4$  and  $13 \pm 2 \text{ kJ/mol}$  for Ar and CH<sub>4</sub>, respectively. As evident from the Polanyi–Wigner equation, the desorption energy and the preexponential factor are strongly coupled. The quoted errors in the desorption energies reflect the uncertainty in determining the preexponential factor during the mathematical inversion of a set of TPD spectra spanning a range of initial coverages.<sup>28</sup> Increasing the coverage beyond  $\sim 0.9 \text{ ML}$  causes the desorption energy to drop, presumably because of compression of the first layer as the chemical potential of the system increases to a value dictated by the thermodynamics of the second layer.<sup>51</sup>

As we demonstrate below, the adsorption of both Ar and CH<sub>4</sub> on MgO(100) does not involve overcoming an activation barrier. Hence, the desorption energies extracted from the TPD experiments are a measure of the adsorbate binding energy to the MgO(100) surface. The binding energetics of both Ar and CH<sub>4</sub> on MgO surfaces have been studied previously using both experimental<sup>35–39</sup> and theoretical methods.<sup>34,35</sup> Our value of  $8.5 \text{ kJ/mol}$  for Ar is in very good agreement with the values determined previously using both LEED adsorption isotherm measurements on MgO(100) ( $9.7 \text{ kJ/mol}$ )<sup>35</sup> and volumetric adsorption isotherm measurements on high-surface-area MgO smokes ( $8.3 \text{ kJ/mol}$ ).<sup>38</sup> Our value of  $13 \text{ kJ/mol}$  for CH<sub>4</sub> is in excellent agreement with the values obtained using specular He scattering on MgO(100) ( $13.6 \text{ kJ/mol}$ )<sup>36</sup> and volumetric adsorption isotherm measurements on high-surface-area MgO smokes ( $14.4$  and  $13.2 \text{ kJ/mol}$ ).<sup>37,39</sup> Theoretical calculations yield adsorption energies of  $9.8$  and  $15.2 \text{ kJ/mol}$  for Ar and CH<sub>4</sub> monolayers on MgO(100), respectively,<sup>34,35</sup> in good agreement with the experimental measurements. Both Ar and CH<sub>4</sub> are weakly bound to the MgO(100) surface. As expected for physisorption, the ratio of the CH<sub>4</sub> to the Ar binding energy ( $\sim 1.53$ ) is nearly identical to the ratio of their polarizabilities ( $1.58$ ).<sup>49</sup>

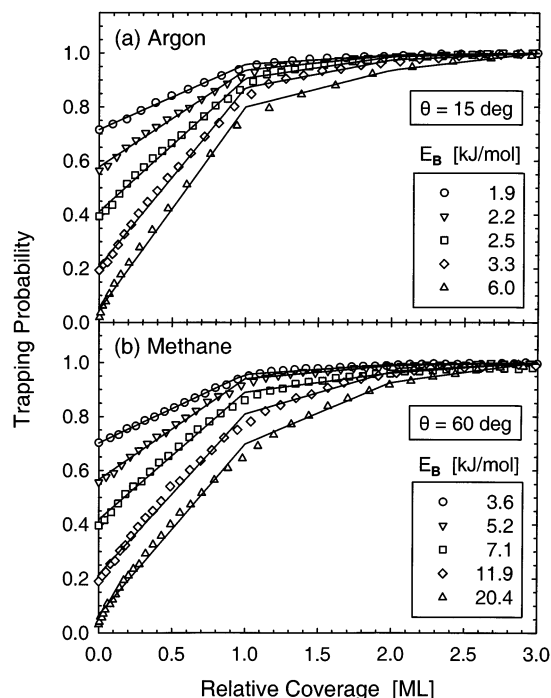


**Figure 3.** Coverage-dependent trapping probabilities of Ar (a) and CH<sub>4</sub> (b) on MgO(100) at 22 K for various incident-beam energies,  $E_B$ , as tabulated. Solid lines represent fits to the adsorbate-assisted trapping model described in the text.

**B. Trapping Dynamics.** The adsorption dynamics of Ar and CH<sub>4</sub> on MgO(100) were studied using molecular beam surface scattering techniques. Specifically, kinetic energy and angle-resolved trapping probabilities were determined using the beam reflection technique of King and Wells.<sup>45</sup> Our implementation of this technique and associated data analysis methods have been described previously.<sup>28,46</sup> We have examined the trapping probability as a function of kinetic energy ( $\sim 2\text{--}20 \text{ kJ/mol}$ ) and incident angle ( $0 \leq \theta \leq 60$ ). For all of the results presented here, the MgO(100) temperature was held constant at 22 K. A limited number of experiments were performed at temperatures above the second layer TPD feature and yielded identical results in the submonolayer coverage regime.

Figure 3 displays a representative subset of analyzed data illustrating the coverage and energy dependence of Ar (Figure 3a) and CH<sub>4</sub> (Figure 3b) trapping on MgO(100) at 22 K. For both Ar and CH<sub>4</sub>, the trapping probability decreases with increasing kinetic energy and increases with increasing coverage. These general observations are in qualitative agreement with many prior studies of physisorption on metals,<sup>14–16</sup> including a recent report of Ar and CH<sub>4</sub> trapping on Pt(111) at 30 K by Carlsson and Madix.<sup>13</sup> We find that at the highest kinetic energies the trapping probability does not reach unity ( $1.00 \pm 0.02$ ) until completion of the third monolayer.

The observation that the trapping probability increases with increasing coverage indicates that energy transfer between the incident projectile (Ar or CH<sub>4</sub>) and the MgO(100) substrate is less efficient than collisions between the incident projectile and an adsorbed particle of its own kind. Such adsorbate-assisted trapping is a natural consequence of the kinematics and dynamics of collision processes. The adsorption kinetics associated with this mechanism have been described using a modified Kisliuk model in which adsorption may occur only directly or through an *extrinsic* precursor state.<sup>13,14,16</sup> If every particle that traps on a site occupied by an adsorbate migrates to and adsorbs on an unoccupied site in a lower layer prior to



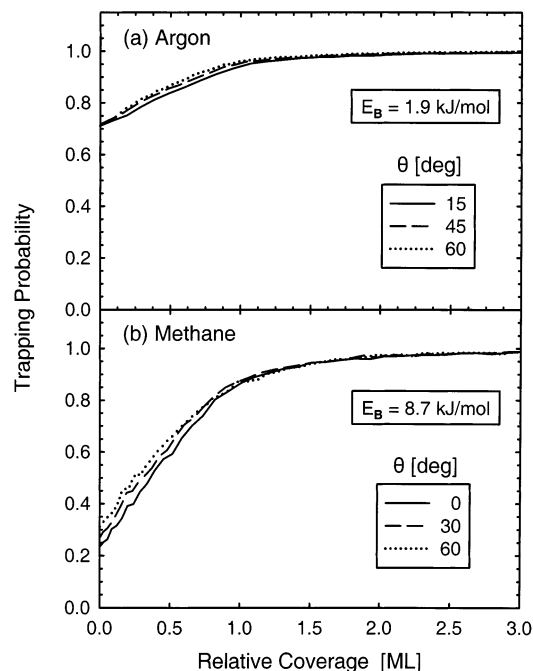


**Figure 4.** Coverage-dependent trapping probabilities for Ar (a) and CH<sub>4</sub> (b) on MgO(100) at 22 K as a function of incident-beam angle,  $\theta$ . For clarity, only a subset of the available data is plotted to illustrate the independence of the trapping probability on  $\theta$ .

desorbing, the trapping dependence can be described by a simple model. This model assumes constant, but different, trapping probabilities on MgO(100) covered by  $n$  (0, 1, 2, ...) layers of the adsorbate with fast intralayer diffusion leading to preferential filling of the lowest layer (highest binding energy) still available for adsorption. This simplified model is equivalent to layer-by-layer growth of the adsorbate overlayer with layer-dependent trapping probabilities. The model can be described mathematically via the following set of Langmuir-like equations:

$$S(\Theta) = S_n(n + 1 - \Theta) + S_{n+1}(\Theta - (n + 1)) \quad \text{for} \\ n \leq \Theta \leq n + 1 \quad (1)$$

where  $S(\Theta)$  is the trapping probability at coverage  $\Theta$ , and  $S_n$  are the trapping probabilities on MgO(100) covered by  $n$  (0, 1, 2, ...) adsorbate layers. The solid lines displayed in Figure 3 represent fits of this simplified layer-by-layer model to the experimental data. In fitting the model to the experimental data,  $S_0$ ,  $S_1$ , and  $S_2$  are fitting parameters and  $S_{n>2}$  is constrained to unity. Clearly, this simple model does a very good job describing the experimental data.

As evident from Figure 3, the initial trapping probability on the bare MgO(100) surface,  $S_0$ , decreases rapidly with increasing kinetic energy. Trapping probabilities on the first,  $S_1$ , and second,  $S_2$ , adsorbate-covered layers also decrease with increasing kinetic energy, albeit in a less dramatic manner. Qualitatively similar behavior is observed for both Ar and CH<sub>4</sub>. The specific details of the trapping dynamics on adsorbate-covered layers, including the quantitative differences between Ar and CH<sub>4</sub>, will be the topic of a future publication and will not be discussed further here.

The dependence of the trapping probability on coverage and incident angle was examined for both Ar and CH<sub>4</sub>. For both species, measurements were performed at five angles (0°, 15°, 30°, 45°, and 60°) and several different kinetic energies. Figure 4 displays a representative subset of the data for Ar (Figure 4a) and CH<sub>4</sub> (Figure 4b). As clearly illustrated, the trapping

probability is independent of incident angle over the entire coverage range ( $0 \leq \Theta \leq 3$  ML). Although not shown specifically here, the coverage-dependent trapping probability is independent of incident angle over the entire range of kinetic energies examined. Hence, the disposal of incident-beam kinetic energy attendant with trapping on the MgO(100) does not depend on the angle at which the impinging Ar and CH<sub>4</sub> particles impact the surface. This finding is in marked contrast to the behavior observed for the initial trapping probability of Ar and CH<sub>4</sub> on Pt(111) for which the trapping probability increases for more oblique impacts.<sup>13</sup>

The dependence of the initial trapping probability,  $S_0$ , on incident angle is often used as a measure of the lateral corrugation<sup>1</sup> of the underlying potential-energy hypersurface, which governs the trapping dynamics. As first demonstrated by Rettner and co-workers,<sup>10</sup> it is often useful to plot angle- and energy-dependent data as a function of an angle-scaled energy,  $E \cos^m(\theta)$ , where  $E$  is the beam kinetic energy,  $\theta$  is the impingement angle of the incident beam measured with respect to the surface normal, and  $m$  is an empirical fitting parameter. The value of  $m$  that best fits the data is often used as a measure of the “smoothness” of the interaction potential. A value of  $m = 2$  corresponds to so-called “normal energy scaling” while a value of  $m = 0$  corresponds to so-called “total energy scaling”. In “normal energy scaling” only translational energy associated with momentum directed perpendicular to the surface is efficiently exchanged during the initial trapping process, whereas in “total energy scaling” both parallel and perpendicular components of the incident projectile’s momentum are equally important in determining the trapping dynamics. In the absence of any lateral corrugation, “normal energy scaling” is obeyed rigorously because parallel momentum is conserved. Conversely, for a highly corrugated interaction, parallel and perpendicular momentum are readily interconverted and the trapping on such a “washboard-like” potential<sup>52</sup> is expected to display “total energy scaling”. Most real systems exhibit behavior intermediate between these two limiting cases.<sup>1</sup>

The angle and kinetic energy dependence of the initial trapping probability of Ar on MgO(100) is displayed in Figure 5 as a function of the angle-scaled energy,  $E \cos^m(\theta)$ . Figure 5 parts a and b show the data plotted as a function of the “total kinetic energy”, ( $m = 0$ ), and “normal kinetic energy”, ( $m = 2$ ), respectively. Clearly, the data exhibit almost perfect “total energy scaling” ( $m = 0 \pm 0.15$ ). As the solid curve in Figure 5a illustrates, the energy dependence of this “total energy scaling” is well-described by the empirical relation  $S(E) = \exp(-a(E - E_0))$ , where  $a = 0.981$  mol/kJ, and  $E_0 = 1.59$  kJ/mol.

The angle and kinetic energy dependence of the initial trapping probability of CH<sub>4</sub> on MgO(100) is displayed in Figure 6 as a function of the angle-scaled energy,  $E \cos^m(\theta)$ . Figure 6 parts a and b show the data plotted as a function of the “total kinetic energy”, ( $m = 0$ ), and “normal kinetic energy”, ( $m = 2$ ), respectively. As in the case of Ar, the CH<sub>4</sub> data exhibit almost perfect “total energy scaling” ( $m = 0 \pm 0.15$ ). As the solid curve in Figure 6a illustrates, the energy dependence of this “total energy scaling” is well-described by the empirical relation  $S(E) = \exp(-a(E - E_0))$ , where  $a = 0.202$  mol/kJ, and  $E_0 = 2.08$  kJ/mol.

As demonstrated above, the adsorption of both Ar and CH<sub>4</sub> on MgO(100) exhibits many similarities with other systems.<sup>13,15,16,29–31</sup> For both species, the adsorption probability increases approximately linearly with increasing coverage indicating that energy transfer between the impinging projectile

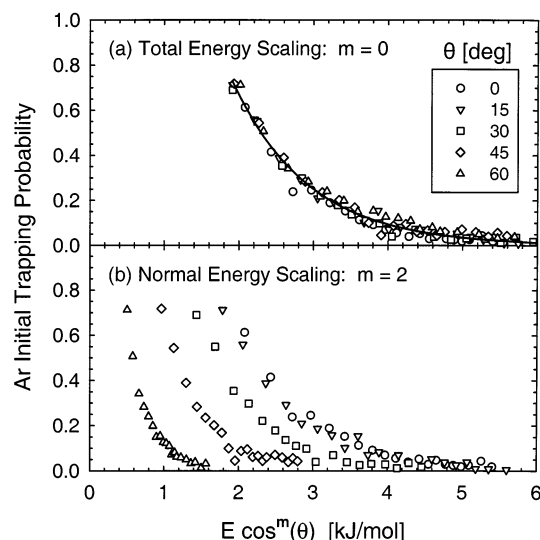


**Figure 5.** Initial trapping probability for Ar on MgO(100) at 22 K as a function of angle-scaled beam kinetic energy,  $E \cos^m(\theta)$ , for various incident-beam angles,  $\theta$ , as tabulated. Data scaled using “total energy scaling”, ( $m = 0$ ), and “normal energy scaling”, ( $m = 2$ ), are plotted in panels a and b, respectively. The solid curve in panel a represents a fit to the empirical relation  $S(E) = \exp(-a(E - E_0))$ , where  $a = 0.981$  mol/kJ and  $E_0 = 1.59$  kJ/mol.

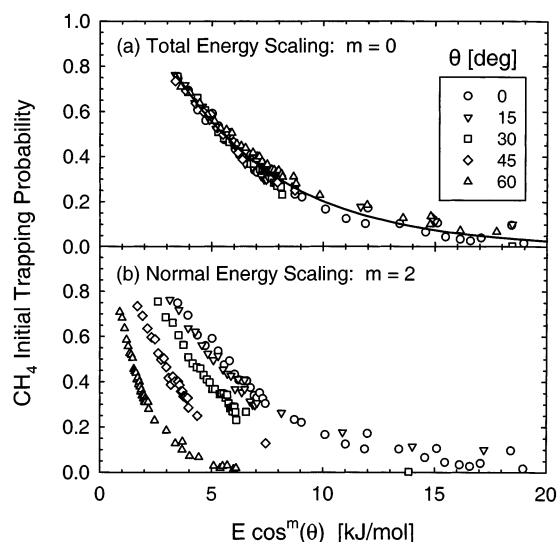


**Figure 6.** Initial trapping probability for CH<sub>4</sub> on MgO(100) at 22 K as a function of angle-scaled beam kinetic energy,  $E \cos^m(\theta)$ , for various incident-beam angles,  $\theta$ , as tabulated. Data scaled using “total energy scaling”, ( $m = 0$ ), and “normal energy scaling”, ( $m = 2$ ), are plotted in panels a and b, respectively. The solid curve in panel a represents a fit to the empirical relation  $S(E) = \exp(-a(E - E_0))$ , where  $a = 0.202$  mol/kJ and  $E_0 = 2.08$  kJ/mol.

and an adsorbed species of its own kind is more efficient than energy transfer between the projectile and the substrate. This process of adsorbate-assisted trapping has been previously observed in other systems.<sup>13,15,16,29–31</sup> The trapping probabilities for both Ar and CH<sub>4</sub> decrease with increasing kinetic energy in a manner qualitatively similar to many other systems as well.<sup>10,15,29,30,53</sup>

The most dramatic difference between the trapping dynamics observed for Ar and CH<sub>4</sub> on MgO(100) and the trapping dynamics typically observed on metals is the dependence of the trapping probability on incident angle. For most metal systems, the trapping probability increases with increasing angle, indicating that dissipation of energy associated with momentum

directed toward the surface is more facile and, hence, more important in determining the initial trapping probability.<sup>1</sup> The recent work of Carlsson and Madix<sup>13</sup> in which the initial trapping of Ar and CH<sub>4</sub> on Pt(111) exhibits “normal energy scaling” nicely illustrates this effect. In marked contrast, we find that the initial trapping of Ar and CH<sub>4</sub> on MgO(100) is independent of incident angle and thus displays “total energy scaling”. There are also quantitative differences observed in the energy-dependent trapping probabilities of Ar and CH<sub>4</sub> on Pt(111) and MgO(100). Interestingly, on Pt(111), the energy-dependent trapping probabilities of Ar and CH<sub>4</sub> are nearly identical,<sup>13</sup> whereas on MgO(100), they are markedly different as shown in Figures 5 and 6. At present, we do not have a detailed understanding of these differences but speculate that it may be because both Ar and CH<sub>4</sub> are lighter than Pt, but Ar is heavier than both Mg and O. Scattering calculations should be useful in understanding this phenomenon.

As stated above, the dynamics of molecular adsorption on metal oxides has been largely unexplored. A notable exception is recent studies of CO adsorption on polar surfaces of ZnO by Wöll and co-workers.<sup>29–31</sup> There are many similarities between their findings and ours. Specifically, they find that CO adsorption exhibits adsorbate-assisted trapping and that the initial trapping probability decreases with increasing energy and displays “total energy scaling”. Wöll et al.<sup>29–31</sup> employ specular He scattering to demonstrate that the first  $\sim 0.2$  ML of CO is almost exclusively adsorbed at surface defects. As discussed above, we observe a similar preference for Ar and CH<sub>4</sub> migration to and binding at defects using TPD. Whether the “total energy scaling” observed in the trapping dynamics studies on ZnO and MgO arises from the presence of surface defects or is an intrinsic property of the defect-free materials is uncertain.

While at present the details of the trapping dynamics of atoms and molecules on the surfaces of metal oxides is far from fully understood, there is a relatively large body of data on the structure and energetics of various adsorbates on metal oxides.<sup>26</sup> On the basis of this type of data, it is physically reasonable to expect that the trapping dynamics of adsorbates on metal oxides (and other ionic insulators such as the alkali halides) will exhibit different dynamical behavior than typically observed on metals. For example, most metal oxide (and ionic insulator) surfaces give rise to intense nonspecular He diffraction, whereas most close-packed metal surfaces yield predominantly mirrorlike specular He scattering.<sup>54,55</sup> This difference is due to the large periodic lateral corrugation in the helium–metal oxide interaction potential compared to the relatively smooth helium–metal potential. Both MgO(100)<sup>56</sup> and ZnO(0001)<sup>29,31</sup> exhibit intense He diffraction. The interaction potentials for other adsorbates interacting with metal oxides are also expected to exhibit a large degree of lateral corrugation. For example, recent calculations by Giradet and colleagues indicate that the interaction potentials for both Ar<sup>57</sup> and CH<sub>4</sub><sup>34</sup> with MgO(100) are highly corrugated. Despite the relatively large level of lateral corrugation, adsorbate diffusion is calculated to be facile.<sup>58</sup> Furthermore, the binding energies that we determine for Ar ( $8.5 \pm 1.4$  kJ/mol) and CH<sub>4</sub> ( $13 \pm 2$  kJ/mol) on MgO(100) are in excellent agreement with these theoretical calculations.<sup>34,35</sup>

Upon the basis of the arguments outlined above, it is heuristically reasonable to expect that the adsorption dynamics of atoms and molecules on pristine, well-ordered metal oxide surfaces will exhibit characteristic behavior that differs from that often observed on smooth, close-packed metal surfaces. The dynamical origin of “total energy scaling” observed in recent experimental trapping studies on MgO(100) and ZnO surfaces<sup>29–31</sup>

is not fully understood. Detailed scattering calculations, employing realistic interaction potentials, will prove invaluable in elucidating the effects that intrinsic lateral corrugation and the presence of morphological defects have on the trapping dynamics.

#### IV. Conclusions

The adsorption dynamics and desorption kinetics of Ar and CH<sub>4</sub> on high-quality MgO(100) thin films epitaxially grown on Mo(100) were studied using a combination of molecular beam scattering and temperature-programmed desorption (TPD). Both Ar and CH<sub>4</sub> exhibit an initial trapping probability that decreases dramatically with increasing kinetic energy and is independent of incident angle, indicating that adsorption is a barrierless process obeying "total energy scaling". For both species, the adsorption probability increases approximately linearly with increasing coverage, indicating that energy transfer between the impinging projectile and an adsorbed species of its own kind is more efficient than energy transfer between the projectile and the substrate. This process of adsorbate-assisted trapping suggests the existence of an extrinsic precursor state. The adsorption kinetics through this extrinsic precursor state can be quantitatively described using a simple model based on layer-by-layer growth of the adsorbate overlayer with layer-dependent trapping probabilities. Analysis of the TPD spectra yields desorption energies of  $8.5 \pm 1.4$  and  $13 \pm 2$  kJ/mol for Ar and CH<sub>4</sub>, respectively, in excellent agreement with prior experimental<sup>35–39</sup> and theoretical values.<sup>34,35</sup>

The observation that the initial trapping probabilities for Ar and CH<sub>4</sub> on MgO(100) obey "total energy scaling" is in sharp contrast to recent results<sup>13</sup> for Ar and CH<sub>4</sub> trapping on Pt(111), which exhibit nearly perfect "normal energy scaling". These differences suggest that the adsorbate–substrate interactions on MgO(100) are laterally corrugated, whereas the analogous interactions on Pt(111) are relatively smooth. Despite the presence of a corrugated interaction potential, both Ar and CH<sub>4</sub> are sufficiently mobile on MgO(100) to diffuse to and preferentially bind at morphological defects during a typical TPD experiment. This level of lateral mobility is in agreement with theoretical calculations<sup>58</sup> that indicate facile adsorbate diffusion on the corrugated MgO(100) surface.

**Acknowledgment.** We thank Professor John Tully for his seminal contributions to the field of Surface Dynamics and for many stimulating discussions over the past 20 years. This work was supported by the U.S. Department of Energy Office of Basic Energy Sciences, Chemical Sciences and Materials Sciences Divisions, and it was performed at the W. R. Wiley Environmental Molecular Sciences Laboratory, a national scientific user facility sponsored by the Department of Energy's Office of Biological and Environmental Research and located at Pacific Northwest National Laboratory. Pacific Northwest National Laboratory is operated for the U.S. Department of Energy by Battelle under Contract No. DE-AC06-76RLO 1830.

#### References and Notes

- (1) Kindt, J. T.; Tully, J. C. *Surf. Sci.* **2001**, *477*, 149.
- (2) Rettner, C. T.; Auerbach, D. J.; Tully, J. C.; Kleyn, A. W. *J. Phys. Chem.* **1996**, *100*, 13021.
- (3) Tully, J. C. *Surf. Sci.* **1994**, *300*, 667.
- (4) Head-Gordon, M.; Tully, J. C. *Surf. Sci.* **1992**, *268*, 113.
- (5) Head-Gordon, M.; Tully, J. C.; Schlichting, H.; Menzel, D. *J. Chem. Phys.* **1991**, *95*, 9266.
- (6) Schlichting, H.; Menzel, D.; Brunner, T.; Brenig, W.; Tully, J. C. *Phys. Rev. Lett.* **1988**, *60*, 2515.
- (7) Tully, J. C. *Surf. Sci.* **1981**, *111*, 461.
- (8) Head-Gordon, M.; Tully, J. C.; Rettner, C. T.; Mullins, C. B.; Auerbach, D. J. *J. Chem. Phys.* **1991**, *94*, 1516.
- (9) Mullins, C. B.; Rettner, C. T.; Auerbach, D. J.; Weinberg, W. H. *Chem. Phys. Lett.* **1989**, *163*, 111.
- (10) Rettner, C. T.; Bethune, D. S.; Auerbach, D. J. *J. Chem. Phys.* **1989**, *91*, 1942.
- (11) Rettner, C. T.; Schweizer, E. K.; Mullins, C. B. *J. Chem. Phys.* **1989**, *90*, 3800.
- (12) Smith, R. J.; Kara, A.; Holloway, S. *Surf. Sci.* **1993**, *281*, 296.
- (13) Carlsson, A. F.; Madix, R. J. *Surf. Sci.* **2000**, *458*, 91.
- (14) Arumainayagam, C. R.; McMaster, M. C.; Madix, R. J. *J. Vac. Sci. Technol., A* **1991**, *9*, 1581.
- (15) Arumainayagam, C. R.; Madix, R. J.; McMaster, M. C.; Suzawa, V. M.; Tully, J. C. *Surf. Sci.* **1990**, *226*, 180.
- (16) Kang, H. C.; Mullins, C. B.; Weinberg, W. H. *J. Chem. Phys.* **1990**, *92*, 1397.
- (17) Rettner, C. T.; Michelsen, H. A.; Auerbach, D. J. *J. Chem. Phys.* **1995**, *102*, 4625.
- (18) Michelsen, H. A.; Rettner, C. T.; Auerbach, D. J.; Zare, R. N. *J. Chem. Phys.* **1993**, *98*, 8294.
- (19) Rettner, C. T.; Auerbach, D. J.; Michelsen, H. A. *Phys. Rev. Lett.* **1992**, *68*, 1164.
- (20) Rettner, C. T.; Pfnur, H. E.; Auerbach, D. J. *Phys. Rev. Lett.* **1985**, *54*, 2716.
- (21) Kinnersley, A. D.; Darling, G. R.; Holloway, S.; Hammer, B. *Surf. Sci.* **1996**, *364*, 219.
- (22) Darling, G. R.; Holloway, S. *Rep. Prog. Phys.* **1995**, *58*, 1595.
- (23) Seets, D. C.; Reeves, C. T.; Ferguson, B. A.; Wheeler, M. C.; Mullins, C. B. *J. Chem. Phys.* **1997**, *107*, 10229.
- (24) Davis, J. E.; Nolan, P. D.; Karseboom, S. G.; Mullins, C. B. *J. Chem. Phys.* **1997**, *107*, 943.
- (25) Verhoef, R. W.; Kelly, D.; Mullins, C. B.; Weinberg, W. H. *Surf. Sci.* **1994**, *311*, 196.
- (26) Henrich, V. E.; Cox, P. A. *The Surface Science of Metal Oxides*; Cambridge University Press: New York, 1994.
- (27) Stimman, M. J.; Huang, C.; Smith, R. S.; Joyce, S. A.; Kay, B. D. *J. Chem. Phys.* **1996**, *105*, 1295.
- (28) Dohnálek, Z.; Kimmel, G. A.; Joyce, S. A.; Ayotte, P.; Smith, R. S.; Kay, B. D. *J. Phys. Chem. B* **2001**, *105*, 3747.
- (29) Becker, T.; Kunat, M.; Boas, C.; Burghaus, U.; Wöll, C. *J. Chem. Phys.* **2000**, *113*, 6334.
- (30) Becker, T.; Boas, C.; Burghaus, U.; Wöll, C. *J. Vac. Sci. Technol., A* **2000**, *18*, 1089.
- (31) Becker, T.; Boas, C.; Burghaus, U.; Wöll, C. *Phys. Rev. B* **2000**, *61*, 4538.
- (32) Wu, M.-C.; Corneille, J. S.; He, J.-W.; Estrada, C. A.; Goodman, D. W. *J. Vac. Sci. Technol., A* **1992**, *10*, 1467.
- (33) Wu, M.-C.; Corneille, J. S.; Estrada, C. A.; He, J.-W.; Goodman, D. W. *Chem. Phys. Lett.* **1991**, *182*, 472.
- (34) Picaud, S.; Girardet, C.; Duhoo, T.; Lemoine, D. *Phys. Rev. B* **1999**, *60*, 8333.
- (35) Meichel, T.; Suzanne, J.; Girard, C.; Girardet, C. *Phys. Rev. B* **1988**, *38*, 3781.
- (36) Jung, D. R.; Cui, J. H.; Frankl, D. R. *Phys. Rev. B* **1991**, *43*, 10042.
- (37) Madih, K. Ph.D. Thesis, Université d'Aix-Marseille, Marseille, France, 1986.
- (38) Coulomb, J. P.; Sullivan, T. S.; Vilches, O. E. *Phys. Rev. B* **1984**, *30*, 4753.
- (39) Freitag, A.; Larese, J. Z. *Phys. Rev. B* **2000**, *62*, 8360.
- (40) Grunze, M.; Ruppender, H.; Elshazly, O. *J. Vac. Sci. Technol., A* **1988**, *6*, 1266.
- (41) Schlichting, H.; Menzel, D. *Rev. Sci. Instrum.* **1993**, *64*, 2013.
- (42) Kay, B. D. Unpublished work.
- (43) Auerbach, D. J. Velocity Measurements by Time-of-flight Methods. In *Atomic and Molecular Beam Methods*; Scoles, G., Ed.; Oxford University Press: New York, 1988; Vol. 1, pp 362–379.
- (44) Kay, B. D.; Raymond, T. D.; Rice, J. K. *Rev. Sci. Instrum.* **1986**, *57*, 2266.
- (45) King, D. A.; Wells, M. G. *Surf. Sci.* **1972**, *29*, 454.
- (46) Brown, D. E.; George, S. M.; Huang, C.; Wong, E. K. L.; Rider, K. B.; Smith, R. S.; Kay, B. D. *J. Phys. Chem.* **1996**, *100*, 4988.
- (47) Dohnálek, Z.; Kimmel, G. A.; McCreedy, D. E.; Young, J. S.; Dohnálová, A.; Smith, R. S.; Kay, B. D. *J. Phys. Chem. B* **2002**, *106*, 3526.
- (48) Dohnálek, Z.; Smith, R. S.; Kay, B. D. Unpublished work.
- (49) *CRC Handbook of Chemistry and Physics*, 80<sup>th</sup> ed.; CRC Press: New York, 1999.
- (50) de Jong, A. M.; Niemantsverdriet, J. W. *Surf. Sci.* **1990**, *233*, 355.

- (51) Bruch, L. W.; Cole, M. W.; Zaremba, E. *Physical Adsorption: Forces and Phenomena*; Clarendon Press: Oxford, U.K., 1997.
- (52) Tully, J. C. *J. Chem. Phys.* **1990**, *92*, 680.
- (53) Madix, R. J.; Carlsson, A.; Kao, C. L. *Abstr. Pap. — Am. Chem. Soc.* **2000**, *219*, 34-COLL.
- (54) Boato, G. Elastic Scattering of Atoms. In *Atomic and Molecular Beam Methods*; Scoles, G., Ed.; Oxford University Press: New York, 1992; Vol. 2, pp 340–365.
- (55) Comsa, G.; Poelsema, B. Scattering from Disordered Surfaces. In *Atomic and Molecular Beam Methods*; Scoles, G., Ed.; Oxford University Press: New York, 1992; Vol. 2, pp 463–487.
- (56) Benedek, G.; Brusdeylins, G.; Senz, V.; Skofronick, J. G.; Toennies, J. P.; Traeger, F.; Vollmer, R. *Phys. Rev. B* **2001**, *6412*, 5421.
- (57) Briquez, S.; Girardet, C.; Goniakowski, J.; Noguera, C. *J. Chem. Phys.* **1996**, *105*, 678.
- (58) Lakhli, A.; Girardet, C. *J. Chem. Phys.* **1991**, *94*, 688.